Effect of shear rupture on aggregate scale formation in sea ice

Article

Published Version

It is advisable to refer to the publisher's version if you intend to cite from the work. See Guidance on citing.

To link to this article DOI: http://dx.doi.org/10.1029/2009JC006043

Publisher: American Geophysical Union

www.reading.ac.uk/centaur

CentAUR

Central Archive at the University of Reading

Reading's research outputs online

Effect of shear rupture on aggregate scale formation in sea ice

Alexander V. Wilchinsky,[1] Daniel L. Feltham,[1,2] and Mark A. Hopkins[3]

[1]   A discrete element model is used to study shear rupture of sea ice under convergent wind stresses. The model includes compressive, tensile, and shear rupture of viscous elastic joints connecting floes that move under the action of the wind stresses. The adopted shear rupture is governed by Coulomb's criterion. The ice pack is a 400 km long square domain consisting of 4 km size floes. In the standard case with tensile strength 10 times smaller than the compressive strength, under uniaxial compression the failure regime is mainly shear rupture with the most probable scenario corresponding to that with the minimum failure work. The orientation of cracks delineating formed aggregates is bimodal with the peaks around the angles given by the wing crack theory determining diamond-shaped blocks. The ice block (floe aggregate) size decreases as the wind stress gradient increases since the elastic strain energy grows faster leading to a higher speed of crack propagation. As the tensile strength grows, shear rupture becomes harder to attain and compressive failure becomes equally important leading to elongation of blocks perpendicular to the compression direction and the blocks grow larger. In the standard case, as the wind stress confinement ratio increases the failure mode changes at a confinement ratio within 0.2–0.4, which corresponds to the analytical critical confinement ratio of 0.32. Below this value, the cracks are bimodal delineating diamond shape aggregates, while above this value failure becomes isotropic and is determined by small-scale stress anomalies due to irregularities in floe shape.

Citation: Wilchinsky, A. V., D. L. Feltham, and M. A. Hopkins (2010), Effect of shear rupture on aggregate scale formation in sea ice, *J. Geophys. Res.*, *115*, C10002, doi:10.1029/2009JC006043.

1.   Introduction

[2]   In the polar oceans, seawater freezes to form sea ice of several meters thickness that can cover up to $15 \cdot 10^6$ km^2 in the Arctic and $20 \cdot 10^6$ km^2 in the Antarctic. Sea ice plays a significant role in determining polar and global climate and Global Circulation Models (GCMs) used for climate prediction incorporate representations of sea ice dynamics and thermodynamics. Although GCMs use continuum sea ice models, there is strong observational evidence of discontinuous sea ice dynamics. At the scale of sea ice floes, deformation is concentrated in leads and ridges but discontinuous deformation is also observed in bands that extend from tens to thousands of kilometers, as illustrated in 3 year deformation maps over the western basin by *Kwok* [2001]. Such bands are usually referred to as slip lines [*Erlingsson*, 1991; *Overland et al.*, 1998] or linear kinematic features [*Kwok*, 2001]. The slip lines frequently intersect at acute angles apparently independent of the spatial scale [*Walter et al.*, 1995; *Weiss*, 2001] and delineate regions of approximately diamond-shaped floe aggregates.

[3]   The floe aggregates, which we shall refer to as blocks, consist of floes frozen together. *Wilchinsky and Feltham* [2006] developed a model of sea ice dynamics that treated the ice cover as a collection of diamond-shaped blocks. In this theory, the rheology of the ice cover depended upon the orientation of the diamonds, which was allowed to evolve according to kinematic and mechanical processes, including fracturing. Here, we focus on the initial formation of the blocks, i.e., the fracturing of an ensemble of frozen-together floes into floe aggregates. We follow *Hopkins et al.* [2004], who studied the fracture of a sea ice cover using a discrete element model that considered compressive and tensile failure of interfloe joints as floe move under an applied wind stress. When a crack starts to form, a relaxation wave travels outward and reduces stresses in the surrounding pack. *Hopkins et al.* [2004] found, under typical wind stress patterns, that the model produced rectilinear blocks, in contrast to the observed diamond-shaped blocks.

[4]   It has been argued [e.g., *Schulson*, 2001; *Weiss and Schulson*, 2009], based upon a strong similarity between sea ice leads and wing cracks observed in the laboratory, that slip lines form through a mechanism of shear rupture, i.e., failure/crack formation once sufficient shear stress is reached. We accordingly extend the study of *Hopkins et al.* [2004] by incorporating into the discrete element model a representation of shear rupture. We find that the modified discrete element model now reproduces

[1]Centre for Polar Observation and Modelling, National Centre for Earth Observation, University College London, London, UK.
[2]British Antarctic Survey, Cambridge, UK.
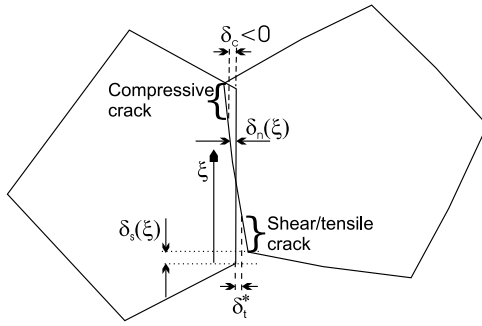[3]CRREL, U.S. Army Corps of Engineers, Hanover, USA.

Figure 1. Adjacent floe interaction.

the observed diamond-shaped blocks under typical wind stress patterns.

[5] The discrete element model, model of shear rupture, wind forcing, and configuration of the numerical experiments is described in section 2. In section 3, the discrete element simulations of block formation are presented and the results discussed in terms of the controls on the block size and shape: subsection 3.1 describes uniaxial compression with varying wind stress; subsection 3.2 describes uniaxial compression with varying tensile strength; and subsection 3.3 describes biaxial compression as the confinement ratio is altered. Our main conclusions are summarized in section 4.

2. Model Configuration

[6] We use a discrete element sea ice model originally developed by *Hopkins* [1996] and expanded by *Hopkins et al.* [2004]. *Hopkins et al.* [2004] used the model to study fracture of a sea ice cover due to compressive and tensile failure under the action of wind stress, and we will closely follow this paper's methodology, where details about the model can be found. The model parameters used are summarized in Table 1. In particular the elastic modulus and Poisson ratio are around the values given by *Evans and Untersteiner* [1971]. The ice pack is 400 km in size and consists of a tiling of typically 4 km wide ice floes whose shape is produced by a Voronoi tessellation. Initially the floes are connected by frozen joints with a viscous-elastic rheology. The mean thickness of the floes is 3 m and the new ice thickness determining the compressive strength of the joints between the floes is 0.25 m. The floes are considered to be rigid and any deformation at the joints is determined by mutual motion of the adjacent edges of neighboring floes. The joints can sustain compressive, tensile and shear forces. It is assumed that the mutual floe displacement $\delta = (\delta_n, \delta_s)$ (normal and tangential to the joint, Figure 1) is distributed over the whole floe average length L so that the normal and shear stresses at a joint are given by

$$\sigma_n = \frac{hE\delta_n}{L} \equiv k_n\delta_n, \tag{1}$$

$$\sigma_s = \frac{hG\delta_s}{L} \equiv k_s\delta_s, \tag{2}$$

where E is the compressive elastic modulus, $G = E/[2(1 + \nu)]$ is the shear modulus where ν is Poisson's ratio, and h is the

mean ice thickness. Note that $k_n/k_s = 2(1 + \nu)$. The elastic stress is combined with a viscous stress, included to damp elastic waves and model inelasticity of the ice. *Hopkins et al.* [2004] used only tensile and compressive failure regimes of the joints. The compressive failure stress (strength) σ_c is based on unconfined buckling [*Kovacs and Sodhi*, 1980],

$$\sigma_c = -1285h_{\min}^{3/2} \text{ kPa m} = -160.625 \text{ kPa m}, \tag{3}$$

for $h_{\min} = 0.25$ m.

[7] The model also requires imposing a tensile strength at a joint, σ_t which should already account for the joint thickness $h_{\min}$. Laboratory experiments by *Richter-Menge and Jones* [1993] showed that sea ice tensile strength significantly depends on temperature and porosity and can vary from 0.2 MPa at $-3°$C up to 0.78 MPa at $-20°$C. *Dempsey et al.* [1999] considered a crack propagation experiment on a block of ice 0.5–80 m wide and concluded that the tensile strength depends on this floe scale as $0.59/(1 + L/0.26)^{1/2}$ MPa and could range from 0.05 MPa for an 80 m wide floe up to 0.5 MPa for a 0.5 m wide floe. This shows a high sensitivity of the ice tensile strength to its temperature and structure, e.g., crack density, without knowing which such idealized experimental results cannot directly be applied to our model. Assuming only one crack per joint (typically 4 km long) would determine only the lower limit of 5.5 kPa for the tensile strength. During the Sea Ice Mechanics Initiative study on a 1.42 m thick floe, *Lewis and Richter-Menge* [1998] recorded tensile stresses up to 80 kPa. *Weiss and Schulson* [2007] plotted stresses recorded during SHE-BA expedition and found the largest tensile stresses to be 50 kPa, which would determine $\sigma_t = 12.5$ kPa m for $h_{\min} = 0.25$ m. For our standard case scenario we choose the tensile failure stress (strength) of the joints σ_t to be 10 times smaller than the compressive strength as this produces block shapes similar to those usually observed. However, we also perform simulations in which we vary the tensile strength between 0.1 and 1 times the compression strength, which includes the median value of *Richter-Menge and Jones* [1993]. We relate the compressive and tensile strengths through a parameter r, $\sigma_t = -r\sigma_c$, not because there is any physical evidence of a linear dependence between the compressive and tensile strengths, but because, as will be seen from our calculations, the ratio

Table 1. Model Parameters

| Parameter	Symbol	Value
Average floe thickness	h	3 m
Minimum ice thickness	$h_{\min}$	0.25 m
Average floe size	L	4 km
Pack width	L_d	400 km
Elastic modulus	E	1 GPa
Poisson ratio	ν	0.3
Ice compressive strength	σ_c	$1285h_{\min}^{3/2}$ kPa m
Ice tensile strength	σ_t	$-r\sigma_c$, $r = 0.1$ (standard case)
Ice density	ρ_i	920 kg m^{-3}
Air density	ρ_a	1.2 kg m^{-3}
Seawater density	ρ_w	1010 kg m^{-3}
Air and water drag coefficients		0.0012, 0.0055
Shear rupture coefficient	μ	0.6 (standard case)
Ice sliding friction coefficient	k	0.32
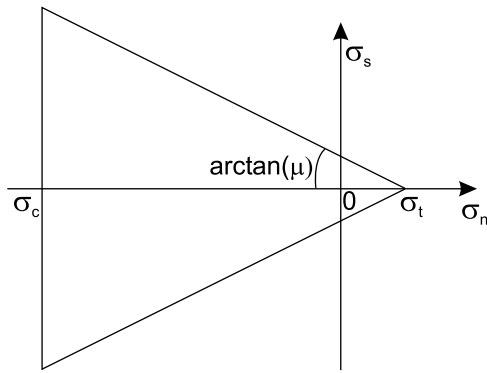
Figure 2. Failure criterion for the joints.

between σ_t and σ_c, expressed through r, crucially determines the model behavior.

[8] In the original model of *Hopkins et al.* [2004] as the mutual floe displacement increases, the joint stress increases proportionally, and when the stress reaches the failure stress, the joint starts to fail. As the displacement increases further, the stress decreases (weakens) linearly until it reaches zero and a crack is formed locally. When a crack extends beyond 95% of the joint length, the joint fails. After this the floe edges can separate forming a lead or overlap making a ridge with the ridging force determined by *Hopkins* [1994] as $F = 928h_{min}^2 l + 26126h_{min}$ (in N per meter along the ridge), where l is the length of ice pushed into the ridge.

[9] The ice sliding friction coefficient is taken here as 0.32 as was shown by several meter scale rafting experiments [*Hopkins and Tuhkuri*, 1999]. This value of the sliding coefficient is smaller than the static coefficient of friction found by *Schulson et al.* [2006] over a Coulombic fault, where the typical values were in the range 0.7–0.9. However, the latter were measured on a scale which is small in comparison with the floe scale, and we expect small-scale anomalies to reduce due to abrasion and their effect to be less prominent. Indeed, *Schulson et al.* [2006] state that their measured static coefficient of friction is greater than the kinetic coefficient of friction. Several meter scale floe edge sliding experiments also gave values between 0.3 and 0.4 at velocities when no stick and slip behavior occurred [*Lishman et al.*, 2009]. Generally, the sliding coefficient is expected to play a role only when there is significant interblock sliding, whereas during initial failure of the sea ice cover, which is studied here, its variation was shown by *Hopkins and Thorndike* [2006] not to produce any significant effect.

[10] Here we incorporate a simple model of shear rupture into the discrete element model. Based on laboratory derived fractural failure stress envelopes [*Schulson and Nickolayev*, 1995; *Schulson*, 2001; *Schulson et al.*, 2006], we assume that shear rupture occurs when the tangential (shear) component σ_s of the traction along a joint reaches the Coulomb limit (Figure 2),

$$|\sigma_s| = \mu(\sigma_t - \sigma_n), \quad \sigma_n > \sigma_c, \quad \sigma_n \leq \sigma_t, \quad (4)$$

where σ_n is the normal component of the traction at the joint, and μ is the shear rupture coefficient. Generally μ is

not the slope of the failure envelope expressed in the coordinates of standard stress invariants σ_I and σ_{II}, but if we assume that the stress components along the lead (which are not determined in the model) and across the leads are equal (i.e., $\sigma_{ss} = \sigma_{nn}$, $\sigma_{sn} = \sigma_{ns}$), then μ becomes the same as the slope of the failure envelope in σ_I, σ_{II} coordinates and the results of *Schulson et al.* [2006] imply

$$\mu = \frac{q-1}{q+1}, \quad q = \left[\left(\mu_i^2 + 1 \right)^{1/2} + \mu_i \right]^2, \quad (5)$$

where μ_i is the coefficient of internal friction. Based on stress failure envelopes *Schulson et al.* [2006] obtained mean values $q = 3.48$ at $-3°C$ and $q = 5.69$ at $-10°C$ which correspond to $\mu = 0.55$ and 0.7, respectively. For our calculation we will use a value of 0.6 and also show results as it varies between 0.4 and 1.

[11] The shear rupture criterion (4) assumes a linear Coulomb curve for all shear stresses. Such extension of the linear Coulomb curve until the σ_n axis itself is crossed at a positive tensile joint strength σ_t is a mathematical convenience which leads to collapsing of the common tensile failure truncation onto only one point of zero shear stress at the tip of the envelope ($\sigma_n = \sigma_t$). In this case, the value of tensile strength σ_t is linearly proportional to the cohesive strength (the value of σ_s at $\sigma_n = 0$) through the shear rupture coefficient for the Coulomb failure curve assumed. Analyzing SHEBA stress data *Weiss and Schulson* [2007] showed that the tensile failure strength, which determines the tensile stress truncation, occurs at about $0.8\sigma_t$, and to this level of numerical approximation the value of σ_t can be associated with tensile failure integrated over the joint thickness.

[12] Rearranging (4) we see that given a shear traction component σ_s, the normal traction component determining shear rupture is

$$\sigma_n = \sigma_t - \frac{1}{\mu}|\sigma_s| \equiv \sigma_t^*. \quad (6)$$

Thus the presence of the shear traction effectively modifies the tensile strength to σ_t^*. Note that for high-shear traction components σ_t^* can become compressive (negative). Equation (6) determines a similar relationship between the normal and shear displacements in shear rupture

$$\delta_t^* = \frac{\sigma_t}{k_n} - \frac{k_s}{\mu k_n}|\delta_s|. \quad (7)$$

A joint starts to fail in regions where either the compressive or modified tensile strengths are reached (Figure 1) but the modified tensile strength depends upon the shear traction at the joint and is found at every time step. As it is difficult to implement simultaneous weakening for normal and shear stresses consistently when the normal floe displacement exceeds δ_t^*, we do not incorporate stress weakening and assume in this paper that a crack forms where the elastic stresses reach the failure stresses σ_c or σ_t^*.

[13] The model starts from an initial configuration of floes at rest. The sea ice pack then undergoes deformation under the action of a gradient of wind stress τ, with stress
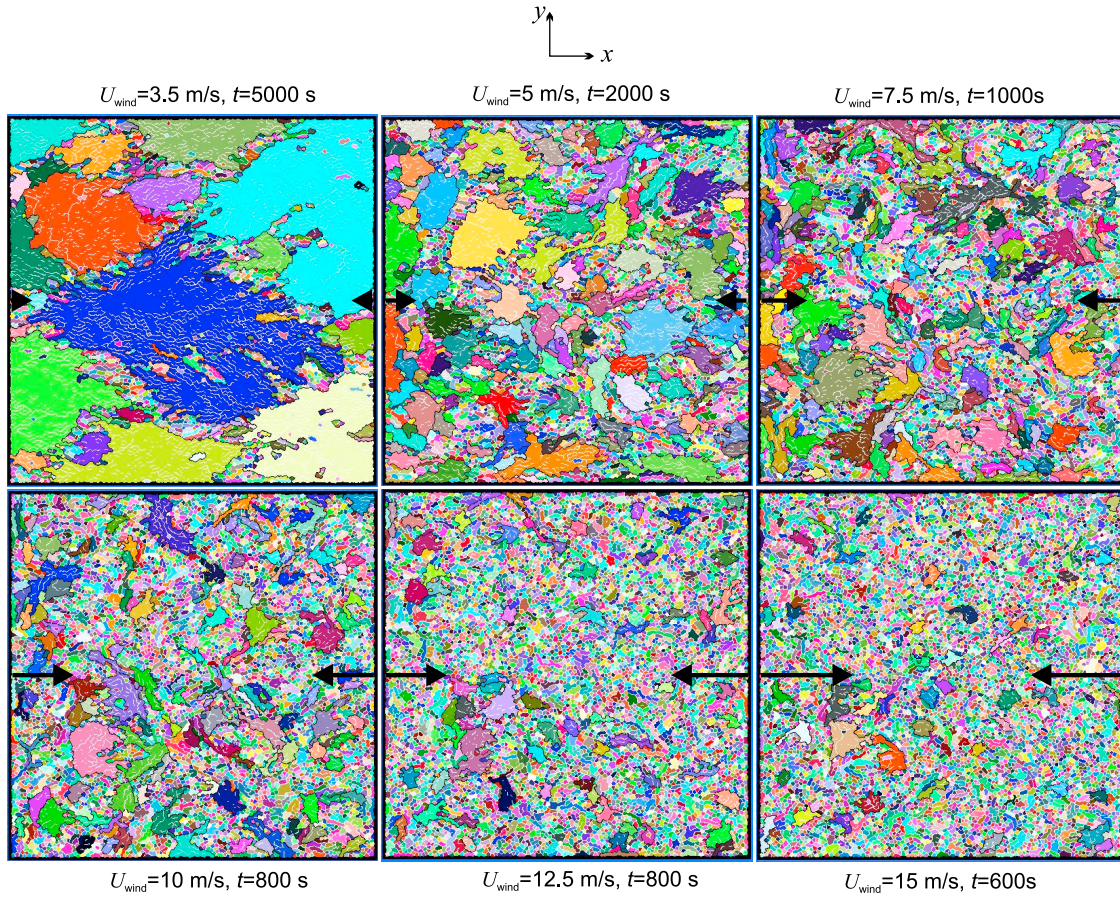
Figure 3. Ice cover for different wind speeds under uniaxial compression. Black color shows joints delineating blocks used in our statistical analysis. The arrows show the compression direction with wind stress gradient being constant across the domain. Cracks filtered out in our statistical analyses are shown in white. The cracks are filtered out to exclude damage zones by retaining only those cracks separating different ice blocks of which at least one is more than ten times the average floe area. We also remove cracks around the rectangular boundary floe joints. Cracks that surround blocks completely contained within another larger block are also filtered out.

varying linearly in the x (eastward) and y (northward) directions,

$$\nabla\tau = 0.0012\rho_a \frac{2U_{wind}^2}{L_d}\mathbf{e}, \qquad (8)$$

where ρ_a is the air density, U_{wind} is the eastward speed of wind blowing at the western end of the model pack, while an equal, but opposite wind blows at the eastern end; L_d is the domain size, and the tensor $\mathbf{e}$ determines the relative values of the wind stress components with $e_{xx} = -1$ and the confinement ratio $R_c = e_{yy}/e_{xx} \leq 1$. The wind drag applied to a floe is

$$\mathbf{F_{wind}} = A\nabla\tau \cdot \left(\mathbf{x} - \frac{1}{2}\mathbf{1}L_d\right), \qquad (9)$$

where A is the floe area, $\mathbf{x}$ is its position, and $\mathbf{1}$ is a unit tensor. The effect of subtracting $\frac{1}{2}L_d$ from the position vector is to make the wind drag symmetrical about the center of the domain. The action of the wind drag force gives rise to a momentum contribution aligned with the force. If the ice pack is homogenous, the linear variation of the wind force leads to the same mutual displacement of all the floes and to a homogenous stress distribution. Boundary effects are minimized by calculating the average stress in the central region and applying it to the boundaries every 10 s. All boundary blocks belonging to the same side of the domain then move simultaneously under the imposed stresses. The time step was $\pi L(\rho_i/E)^{1/2}/8$ ensuring that the energy balance between the wind drag work, fracture energy, inelastic dissipation (including ridge building), frictional dissipation and water drag work has an error of less than 1%.

3. Simulations and Discussion

[14] In the following subsections we present simulations of the break up of the sea ice cover into blocks, or floe aggregates. We analyze and discuss these simulations, focusing on which failure mechanisms dominate, the
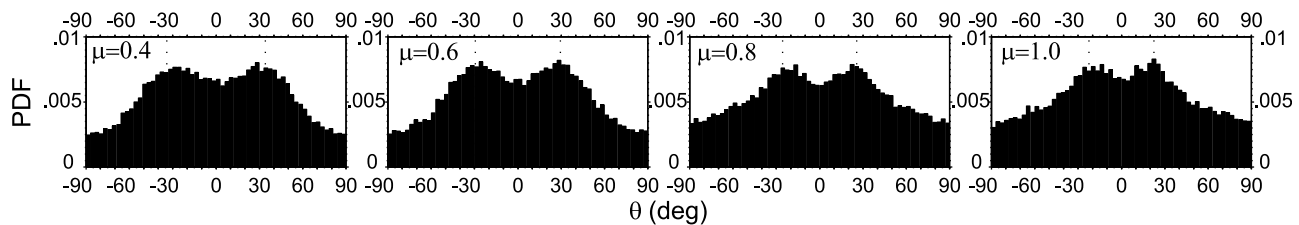
Figure 4. The histograms of the normalized crack length distribution against the angle around the compression direction, x, for different μ under uniaxial compression. The bin width is 3°, and the results are averaged over 10 different initial Voronoi tessellations. The imposed wind speed ranges from 3.5 to 5 m s^{-1} for different μ to ensure the block size is of order 40 km. The cracks are filtered as described in Figure 3. The dotted lines show the critical flaw angle in the wing crack theory determined by $\tan(2\theta) = 1/\mu$ [*Jaeger and Cook*, 1979; *Ashby and Hallam*, 1986; *Schulson*, 2004].

anisotropy of the blocks formed, and the controls on the block size.

3.1. Uniaxial Compression With Variation in Wind Stress

[15] We consider a uniaxial compressive wind stress along axis x, i.e., the only nonzero component of **e** is $e_{xx} = 1$. The wind speeds U_{wind} considered were 3.5, 5, 7.5, 10, 12.5 and 15 m s^{-1}, which correspond to the wind drag gradients of $4.87 \cdot 10^{-8}$, $1.8 \cdot 10^{-7}$, $4.05 \cdot 10^{-7}$, $7.2 \cdot 10^{-7}$, $1.13 \cdot 10^{-6}$ and $1.62 \cdot 10^{-6}$ Pa m^{-1}. For each wind speed the model was run until an established ice block configuration had developed. From the plots of the ice field (Figure 3) it can be seen that the ice cover splits into blocks that are on average elongated along the x axis. The simulation result for $U_{wind} = 3.5$ m s^{-1} especially clearly shows the roughly diamond shape of the blocks. The blocks themselves are permeated by cracks. The model does not include crack refreezing, and some of the cracks could be expected in reality to freeze over, especially those lying within the blocks. From histograms showing the distribution of block-delineating crack length with regard to angle for different values of the shear rupture coefficient μ (Figure 4) we see that the cracks are distributed bimodally around the critical flaw angle in wing-crack formation [*Jaeger and Cook*, 1979; *Ashby and Hallam*, 1986; *Schulson*, 2004],

$$\tan(2\theta) = 1/\mu. \qquad (10)$$

The maxima, however, are not very prominent, presumably due to the limited number of discrete angles determined by the floe edges, along which the critical flaw can only form.

[16] It should be noted that the crack angle is determined by the shear rupture coefficient μ rather than the sliding coefficient k. Equation (10) was derived by considering failure of brittle ice when flaws are present. In this case the resistance to shear at the flaw comes from friction and it is the coefficient of internal friction that should enter (10). In our model, however, the joint stretches elastically until the failure stress is attained. Right before the joint failure, resistance to shearing deformation at the joint coming from its elastic stress is effectively given by the shear failure stress determined by the shear rupture coefficient, so that the latter naturally determines the critical flaw angle (10).

3.1.1. Block Size Distribution

[17] As the block size becomes smaller with increasing wind speed (Figure 5), the block shapes become more erratic as their perimeter is delineated by a relatively small number of joints. This is because the small number of joints prevent the cracks from propagating in certain directions. Similar to *Hopkins and Thorndike* [2006] in Figure 6 we show a cumulative block area distribution function

$$F_A(A) = \frac{N}{A_d} \int_A^\infty P(A)dA, \quad A_d = L_d^2, \qquad (11)$$

where $P(A)$ is the probability distribution function of number of blocks with regard to their area A, and N is the number of blocks within the domain. $F_A(A)$ describes the number of blocks whose area is not smaller than A and generally it looks similar to those found by *Hopkins and Thorndike* [2006]. The most interesting feature is a similar power law distribution for areas less than 300 km^2. However, our results differ as our slope is around -1, while *Hopkins and Thorndike* [2006] obtained -0.68. Other observations show -0.65 [*Rothrock and Thorndike*, 1984], or a range of -0.5 to -0.9 [*Weiss*, 2003], or -0.65 and -0.77 [*Weiss and Marsan*, 2004].

[18] It is difficult to exactly determine the reason for the power law for block area as well as the difference between our result and that of *Hopkins and Thorndike* [2006]. *Weiss and Marsan* [2004] considered a general multifractal model to explain the scale invariance. A power law distribution of ice floe area can be a result of self-similarity such as in the
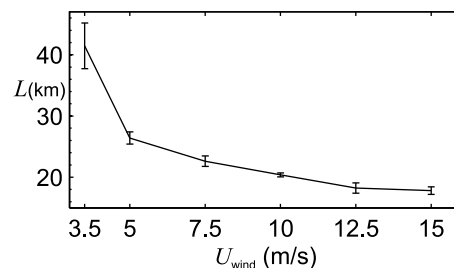

Figure 5. The normalized block size (square root of the block area) for different wind speeds under uniaxial compression. The standard deviation is derived from mean block size for 10 different ice field configurations. Blocks 10 times smaller than the average floe area are filtered out.
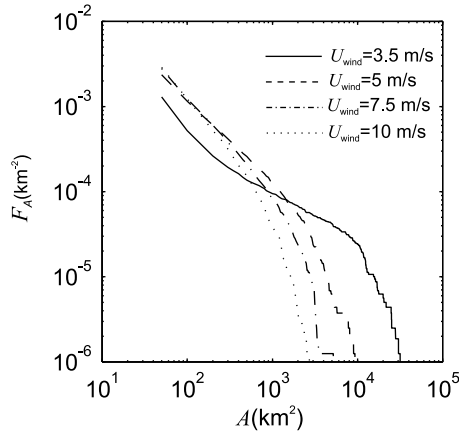
Figure 6. The accumulated block size distribution, F_A (A) for different wind speeds. The curves are averaged over 10 different configurations.

Apollonian gasket [*Rothrock and Thorndike*, 1984]. We, in turn, want to focus on the physics of the process, and consider a very idealized model that could give us some hints on the nature of our block size distribution. The power law distribution is observed at scales less than the mean block sizes (Figure 5), and is effectively independent of the wind stress gradient, apart from the case of U_{wind} = 3.5 m s^{-1} (Figure 6), where the difference probably comes from the block size approaching the domain size.

[19] *Hopkins et al.* [2004] showed that the size of large blocks is determined by the wind stress gradient inducing elastic stress accumulation leading to failure. This will be discussed in more detail in the following subsection. Since the small block size distribution does not depend on the wind stress gradient (Figure 6), we assume that the smaller blocks do not form under the direct action of the wind stress, but rather through the force exerted on their sides by the larger blocks, which leads to the production of damage zones. We illustrate this in Figure 7 where a large block exerts a force F on a side of a region of frozen floes of size D. For simplicity we consider the same failure regime for all the joints. The force is transmitted across the region through the elastic joints, therefore in order for any of the elastic joints to fail all surrounding joints should also approach the same failure strength, e.g., σ_c in compression. Therefore
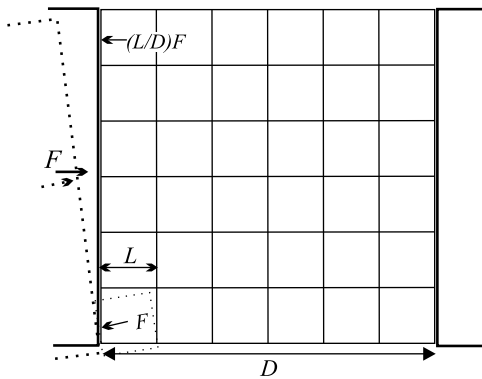

Figure 7. An idealized sea ice area of size D broken up into blocks of size L.

failure of a block of area A would require work linearly proportional to the area A itself. In this case, failure of the region shown in Figure 7 through formation of blocks of size L or just one block of size D requires the same work, while there will be A_D/A_L times more blocks of size L than D, where $A_d = D^2$ and $A_L = L^2$. Since the formation of a block of the floe length L would require A_D/A_L less energy than formation of a block of size D, we shall assume that the formation of a block of area A_L is A_D/A_L times more likely than formation of a block of area A_D. This leads us to conclude that the probability density function of block number must satisfy $P(A_L) = (A_D/A_L)^2\ P(A_D)$, which, after integration, leads to $F_A \propto A^{-1}$ in correspondence with our simulations. It is now necessary to note that under uniaxial compression our model with shear failure produces a two-dimensional failure pattern, while if only compressive failure is modeled (as in the work of *Hopkins and Thorndike* [2006]), a one-dimensional failure pattern is produced, as will be seen in subsection 3.2. In a two-dimensional failure regime, the whole force F can be transmitted onto one small
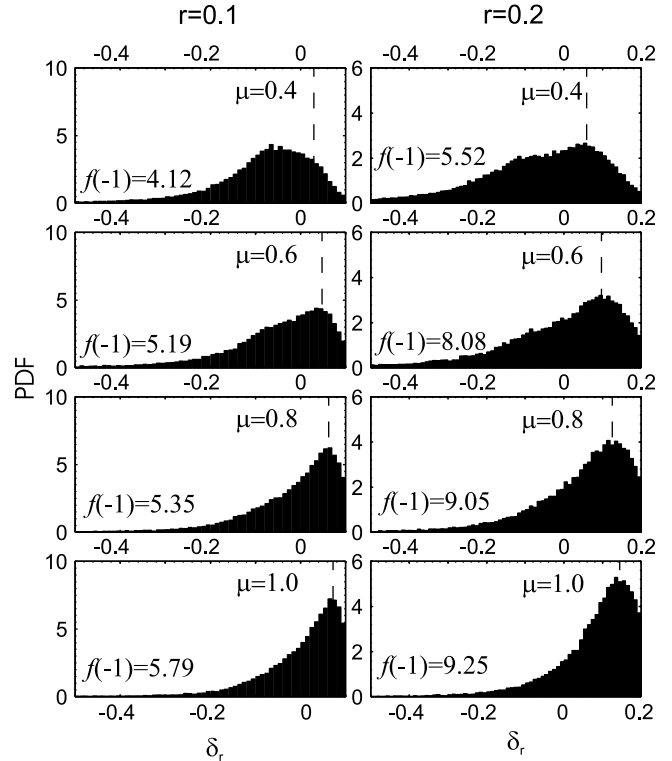

Figure 8. The normalized histogram of the crack length distribution against the normalized tensile failure displacement δ_r for the tensile strength 10 ($r = 0.1$) and 5 ($r = 0.2$) times smaller than the compressive strength for varying μ under uniaxial compression. The bin size is 0.1. The dashed line shows the δ_r values of (15) determining the minimum failure energy. The imposed wind speed ranges from 3.5 to 5 m s^{-1} for different μ to ensure the block size is of order 40 km. The presence of cracks due to compressive failure gives rise to a singular large value of the distribution function at the first histogram bin ($\delta_r = -1$), whose value is shown as $f(-1)$. The cracks are filtered as described in Figure 3.
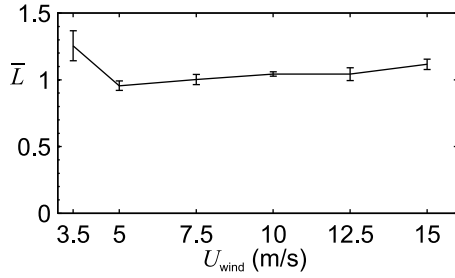
Figure 9. The normalized block size (square root of the block area divided by L_b^s) for different wind speeds under uniaxial compression. The standard deviation is derived from mean block sizes for ten different ice field configurations. Blocks 10 times smaller than the average floe area are filtered out. The estimated block size L_b^s is 33, 27.6, 22.6, 19.5, 17.5, and 16 km for a wind speed of 3.5, 5, 7.5, 10, 12.5, and 15 m s^{-1}, respectively.

block only, whereas in a one-dimensional regime only the force $(L/D)F$ will be transmitted to any one particular block. We account for this by postulating that when the failure regime is one-dimensional, the smaller block is D/L less likely to fail than when the failure regime is two-dimensional. In this case $P(A_D) = (A_D/A_L)^{3/2} P(A_D)$, which

determines $F_A \propto A^{-1/2}$ which is closer to the result of *Hopkins and Thorndike* [2006].

3.1.2. Block Size Evaluation

[20] We follow *Hopkins et al.* [2004] to obtain a rough estimate of the block size under a uniaxial compressive wind stress. While *Hopkins et al.* [2004] considered a one dimensional model under divergence, our failure pattern and the flow motion involved are two-dimensional and more complicated. In particular, as there is no confining stress, under a uniaxial compressive stress gradient the floes are expected to move perpendicular to the compression direction since the floe edges are inclined with respect to the compression direction. Regardless of the direction of motion we estimate the floe speed as $u = |\tau|t/(\rho_i h)$ and the relative floe displacement with the typical floe size of L as

$$\delta = \frac{|\nabla \tau| L}{2\rho_i h} t^2, \quad (12)$$

where $|\nabla \tau| = 0.0024 \rho_a U_{wind}^2/L_d$. The work required to deform a unit length joint by $\delta = (\delta_n, \delta_s)$ is determined by the stresses (1) and (2) as

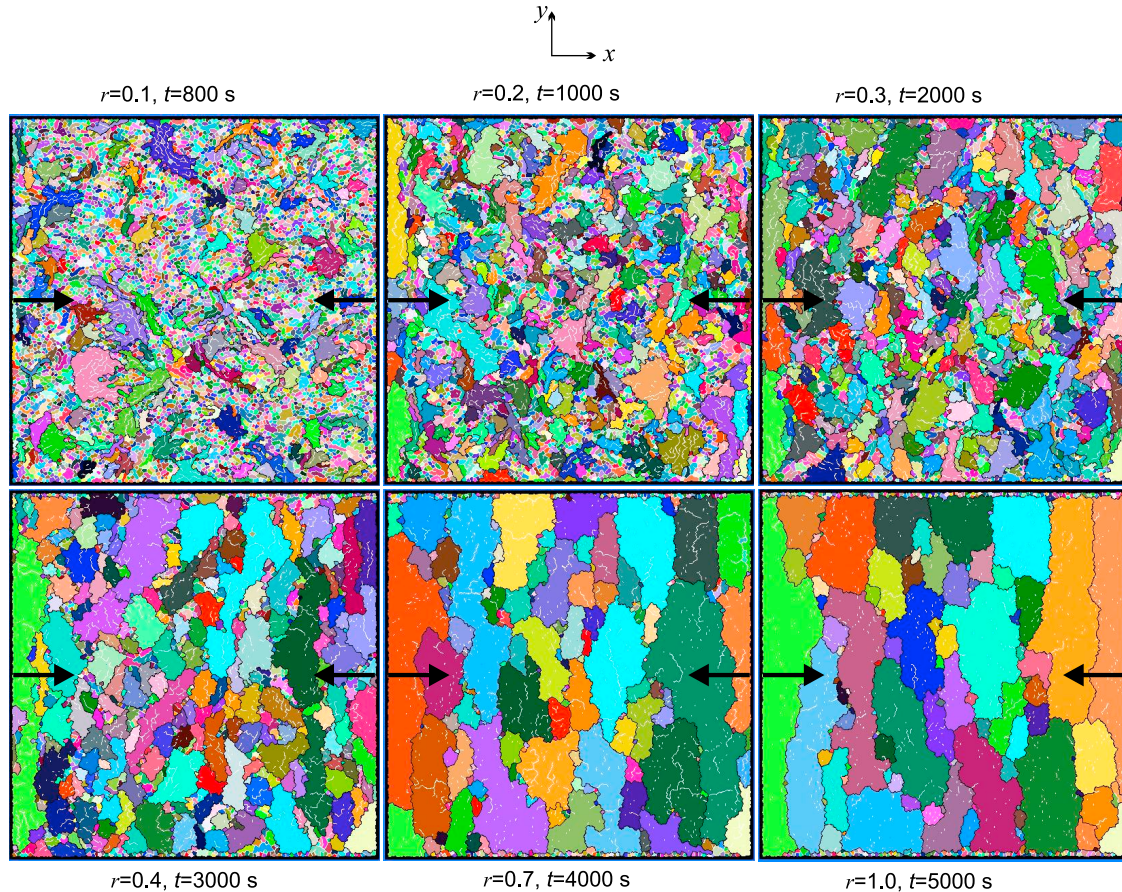$$W = \frac{k_n}{2} \delta_n^2 + \frac{k_s}{2} \delta_s^2. \quad (13)$$

Figure 10. Ice cover for a varying relative tensile strength r and a wind speed of 10 m s^{-1} under uniaxial compression. Joints filtered out in the same way as before are shown in white. The black color shows joints delineating blocks used in our statistical analysis.
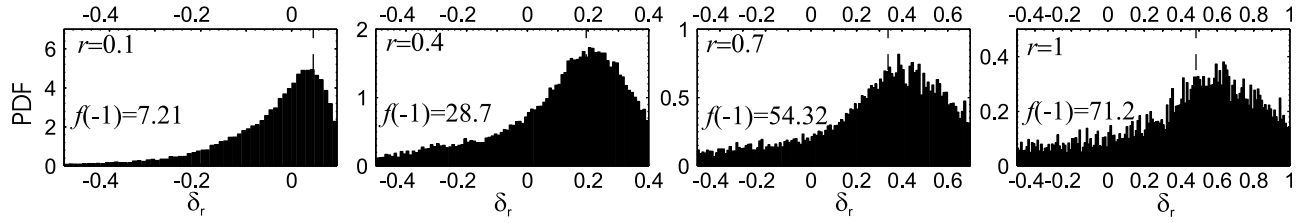
Figure 11. The normalized histogram of the crack length distribution against the normalized tensile failure displacement δ_r for varying relative tensile strength r. The wind speed is 10 m s^{-1} under uniaxial compression. The presence of cracks due to compressive failure gives rise to a singular large value of the distribution function at the first histogram bin ($\delta_r = -1$), whose value is shown as $f(-1)$. The fraction of crack length due to compressive failure is 0.07, 0.29, 0.54, and 0.71 for $r = 0.1, 0.4, 0.7$, and 1, respectively. The same filtering as before is applied.

For a particular δ_n the joint fails when δ_s reaches $\mu(\sigma_t - k_n \delta_n)/k_s$, therefore the failure energy of a unit length crack is

$$W_f = \frac{k_n \delta_n^2}{2} + \frac{\mu^2}{2k_s}(\sigma_t - k_n \delta_n)^2. \qquad (14)$$

The minimum failure energy (at which $dW_f/d\delta_n = 0$) is attained by the following displacements

$$\delta_n^{min} = \frac{2(1+\nu)\mu^2}{1 + 2(1+\nu)\mu^2} \frac{\sigma_t}{k_n}, \qquad (15)$$

$$\delta_s^{min} = \frac{1}{\mu} \delta_n^{min}. \qquad (16)$$

Given a shear stress at a joint, the normal modified tensile strength (6) determines a tensile failure displacement $\delta^*_t = \sigma^*_t/k_n$ that must be reached for the joint to fail. We normalize the tensile failure displacement to $\delta_r = \delta^*_t/|\delta_c|$, where $\delta_c = \sigma_c/k_n$ is the compressive failure displacement. δ_r can be interpreted as a failure regime parameter: for a tensile strength being r times the compressive strength it varies from -1 (pure compressive failure) through 0 (pure shear rupture) to $r > 0$ (pure tensile failure). Figure 8 shows histograms of the normalized crack length distribution during joint failure against δ_r from which it can be seen that the most probable shear rupture regime is determined by minimizing the failure energy W_f. This failure regime involves a tensile shear rupture of the joints through local opening at wing cracks. From (13) we find $d^2W/d\delta_n^2 = k_n[1 + 2(1 + \nu)\mu^2]$, which for $\nu = 0.3$ gives k_n times 1.42, 1.94, 2.66 and 3.6 for $\mu = 0.4, 0.6, 0.8$ and 1, respec-

tively. Therefore as μ decreases the joint failure energy of an arbitrary failure mode differs less from the minimum failure energy, which makes it likelier for the failure mode to deviate from the minimum energy regime. This leads to the histogram peaks smoothing out as μ decreases.

[21] It follows from the simulations presented above that the minimum energy failure mode could be used as the typical failure mode of shear rupture, at least for zero confinement. Due to (12) and (16) we assume that

$$\delta_s = \frac{\nabla \tau L}{2\rho_i h} t^2, \qquad (17)$$

$$\delta_n = \mu \delta_s. \qquad (18)$$

Multiplying the unit length strain energy (13) by the typical joint length L, dividing it by the typical floe area L^2, using (18) and differentiating with regard to time, we can find the rate of change of strain energy per unit area

$$\dot{W} = \frac{k_s + \mu^2 k_n}{2L} \left(\frac{\nabla \tau L}{\rho_i h}\right)^2 t^3. \qquad (19)$$

Given (17) and (18), the failure displacements (15) and (16) are attained at time

$$t_f = \left[\frac{4(1+\nu)\mu}{1 + 2(1+\nu)\mu^2} \frac{\sigma_t}{k_n} \frac{\rho_i h}{\nabla \tau L}\right]^{1/2}. \qquad (20)$$

If we assume that during failure the rate of change of strain energy per unit area $\dot{W}$ is converted into crack failure with
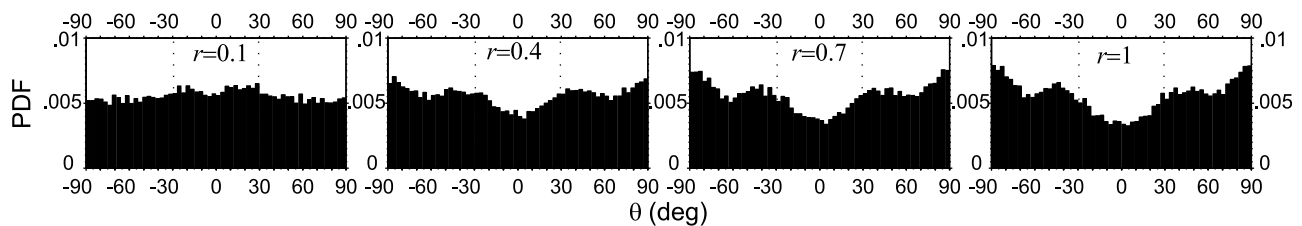

Figure 12. The histograms of the normalized crack length distribution against the angle around the compression direction, x, for varying r and a wind speed of 10 m s^{-1} under uniaxial compression. The same filtering as before is applied.
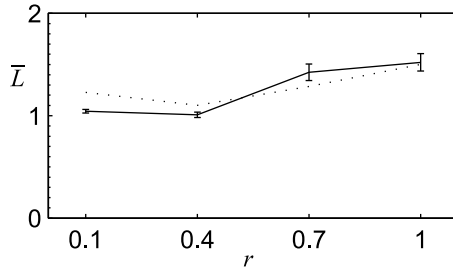
Figure 13. The normalized block size (square root of the block area divided by L_b^s) for varying r under uniaxial compression. The standard deviation is derived from mean block size values for 10 different configurations. Blocks smaller than 10 times the average floe area are filtered out. The estimated block size due to shear rupture only is L_b^s is 19.5, 27.6, 31.8, and 43.7 km for the relative tensile strength $r = 0.1$, 0.4, 0.7, and 1, respectively. The normalized length scale L_b^m with $\alpha = 1.6$ is shown by the dotted line.

failure energy per unit length being W_f, the crack propagation speed per unit area becomes

$$V_f = \frac{\dot{W}}{W_f} = \frac{4}{Lt_f} = \frac{4}{L}\left[\frac{1 + 2(1+\nu)\mu^2}{4(1+\nu)\mu}\frac{E\nabla\tau}{\rho_i\sigma_t}\right]^{1/2}, \quad (21)$$

where we used $k_n = hE/L$ from (1). In a floe train of length L_b^s and unit width, it takes time $2/(L_b^s V_f)$ for a crack to propagate across the unit width, where the factor 2 is introduced in order to account for the bimodality of the crack propagation under a unidirectional wind stress gradient. On the other hand it takes time L_b^s/V_e for the elastic relaxation wave to travel along the train length, where $V_e = (E/\rho_i)^{1/2}$ is the elastic wave speed. When these times are equal, the crack has just enough time to delineate a block without breaking it up further before the elastic stress

disappears through relaxation. Therefore, equating these times we can find the block length scale

$$L_b^s = \left(\frac{2V_e}{V_f}\right)^{1/2} = \left[\frac{(1+\nu)\mu}{1+2(1+\nu)\mu^2}\frac{\sigma_t L^2}{\nabla\tau}\right]^{1/4}. \quad (22)$$

The mean block size normalized by L_b^s is shown in Figure 9 for different wind speeds and is generally close to 1. It is, however, slightly higher for a 3.5 m s^{-1} wind speed as the block size becomes significant relative to the domain size. The number of blocks accounted for as the wind speed approaches 15 m s^{-1} also decreases, as more and more blocks are split by incidental damage of a small number of joints and get filtered out.

3.2. Uniaxial Compression With Variation in Tensile Strength

[22] The ratio of the minimum shear rupture energy (14) to the corresponding compressive failure energy $W_c = k_n\delta_c^2 / 2$ is

$$\frac{W_f}{W_c} = r^2\frac{2(1+\nu)\mu^2}{1 + 2(1+\nu)\mu^2}, \quad (23)$$

where $r = \delta_t/|\delta_c|$ is the normalized tensile strength. As the normalized tensile strength increases, the compressive failure energy W_c (being 200 times larger than the minimum shear rupture energy W_f at $r = 0.1$) gradually becomes comparable with W_f and in particular $W_f/W_c = 0.08$, 0.24 and 0.48 for $r = 0.4$, 0.7 and 1, respectively. Since uniaxial compression is considered, as r increases shear rupture becomes harder to attain, hence compressive failure gradually starts to prevail: the fraction of the total crack length due to compressive failure γ becomes 0.07, 0.29, 0.54 and 0.71 for $r = 0.1$, 0.4, 0.7 and 1, respectively. From the simulation results for the ice field failure (Figure 10) it can be seen that the block size increases with r. The failure regime (δ_r) histogram (Figure 11) shows that failure occurs through the compressive regime
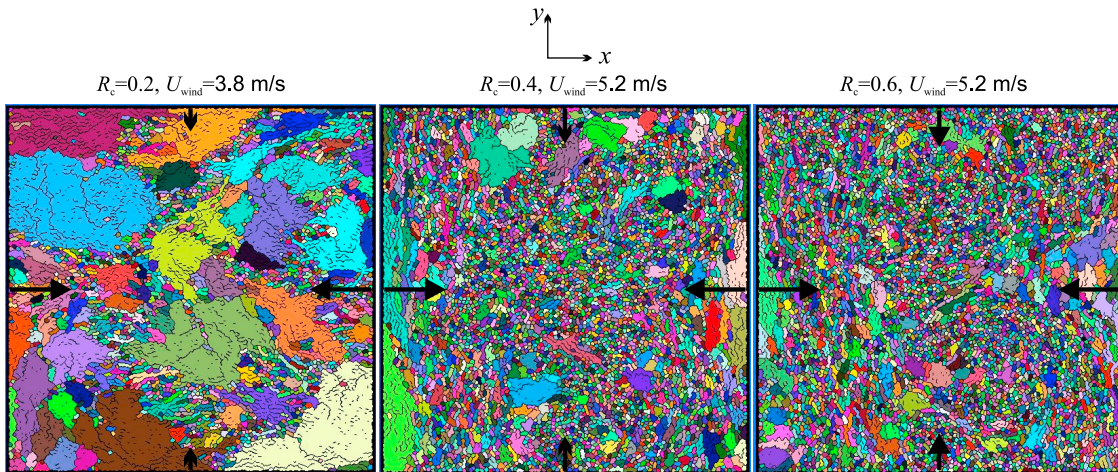

Figure 14. Ice cover for different confinement ratios R_c. Snap shots with $R_c = 0.8$ and 1 are similar to that of $R_c = 0.6$. No filtering was applied. Run duration is 3000 s.
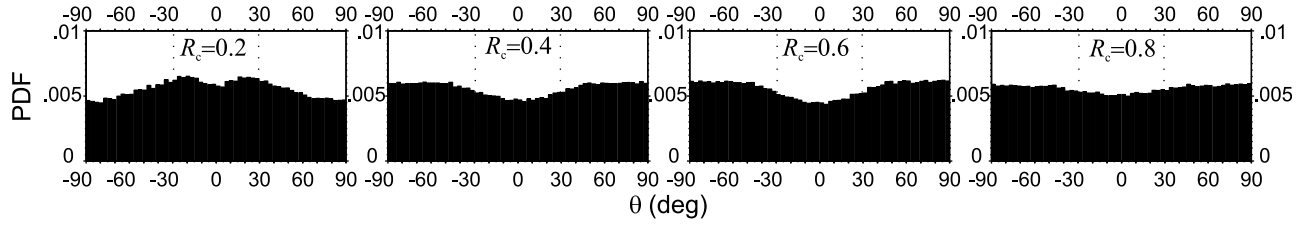
Figure 15. The histograms of the normalized crack length distribution against the angle around the compression direction, x, for varying confinement ratio R_c. The imposed wind speed is 4 m s^{-1} for $R_c = 0.2$ and 5.2 m s^{-1} for the others. The case of $R_c = 1$ is similar to that of $R_c = 0.8$ with even higher uniformity in distribution. No filtering was applied. Run duration is 3000 s.

and shear rupture regime, with a peak situated close to the regime of the minimum shear rupture energy similar to the case of small r. From the crack orientation distribution (Figure 12) it can also be seen that as the normalized tensile strength increases, the failure angle distribution has three local maxima: two at the usual critical flaw angle in wing crack formation, and one perpendicular to the compression direction. Since at $r = 0.1$ the blocks consist of a relatively small number of floes, and there is less possibility for cracks to propagate along a specific direction, the angle distribution is almost uniform in this case. As the block size increases the local maxima in the angle distribution become more pronounced.

[23] The block size normalized by the shear rupture scale L_b^s versus r is shown in Figure 13. The low values of standard deviation in the block size show consistency in the block size formation. The normalized block size increases as r increases. The blocks become elongated perpendicular to the compression direction as the compressive failure mode becomes dominant (as r increases). Due to the high anisotropy of the blocks it is difficult to estimate the block size rigorously, and we will consider a very simple model. The length scale during compressive failure derived by *Hopkins et al.* [2004] takes the following modified form

$$L_b^c = \left(\frac{\sigma_c L^2}{8 \nabla \tau} \right)^{1/4}. \tag{24}$$

(The reason this expression is slightly different from that in the work of *Hopkins et al.* [2004] is that we ignore

strain weakening in this paper.) As the tensile strength increases, compressive failure perpendicular to the compression direction becomes dominant, so that the maximum block scale along the compression direction is given by the compressive failure scale above. If we assume that the shear failure angle θ is determined by (10) then the mean angle of crack propagation would be $\phi = (1 - \gamma) \theta + \gamma \pi / 2$, where γ is the compressive failure fraction discussed above. The across compression direction block scale can then be found as $L_b^a = L_b^c \tan \phi$, which determines the sought length scale of the blocks as the square root of the area of a rhombus with semiaxis lengths L_b^c and $L_b^a : L_b^m = \alpha (L_b^c L_b^a / 2)^{1/2}$, where α accounts for irregularity of both compressive failure, which could be expected to lead to a positive correction to (24) as was found by *Hopkins et al.* [2004], as well as the block shape, which could be more convex than a rhombus due to a nonuniform distribution of compressive and shear failure perpendicular to the compression direction, as can be seen from Figure 10. The normalized values of this block scale L_b^m / L_b^s with $\alpha = 1.6$ are presented in Figure 13 as a dashed line. It can be seen that for $r \leq 0.4$ the block size is properly described by the shear rupture scale L_b^s as the block size is mainly determined by the shear rupture mechanism. As the normalized tensile strength r increases, despite some quantitative difference, the found block size scale L_b^m describes the block length change rather well. Increasing of r beyond unity was not considered as this would make the block length become comparable with the domain size.
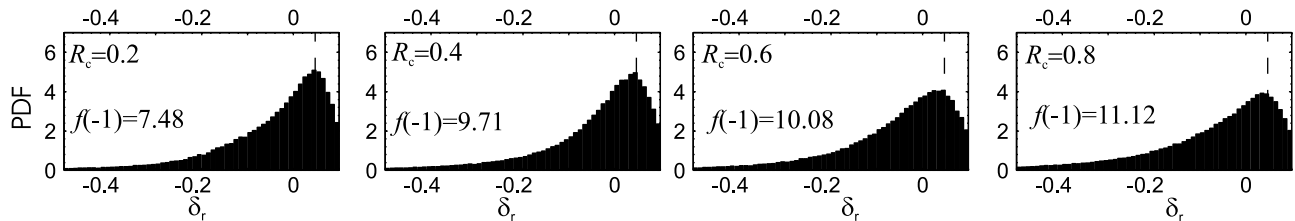

Figure 16. The normalized histogram of the crack length distribution with regard to the normalized tensile failure displacement δ_r for varying confinement ratio R_c. The imposed wind speed is 4 m s^{-1} for $R_c = 0.2$ and 5.2 m s^{-1} for the others. The presence of cracks due to compressive failure gives rise to a singular large value of the distribution function at the first histogram bin ($\delta_r = -1$), whose value is shown as $f(-1)$. The fraction of crack length due to compressive failure is 0.07, 0.1, 0.1, and 0.11 for $R_c = 0.2$, 0.4, 0.6, and 0.8, respectively. The case of $R_c = 1$ is similar to that of $R_c = 0.8$. The dashed line shows the δ_r values of (15) determining the minimum failure work. No filtering was applied.
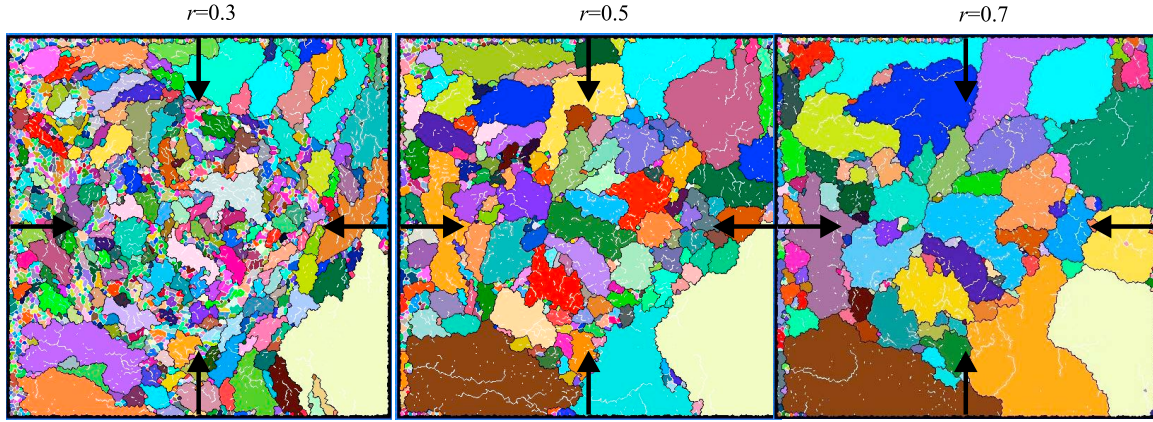
Figure 17. Ice cover for purely convergent wind stress ($R_c = 1$) and varying tensile strength r. The wind speed is 5 m s^{-1}. Run duration is 3000 s.

3.3. Confinement Ratio Variation Under Compression

[24] Here we fix the wind stress gradient along axis x and vary the compressive stress in the perpendicular direction along axis y. The confinement ratio R_c is the ratio between the principal wind stress gradients components, $R_c = \nabla \tau_{yy}/\nabla \tau_{xx} = e_{yy}/e_{xx}$, so that the stress gradient variation comes from imposing $e_{yy} = R_c$, $e_{xx} = 1$ in (8). We consider our standard case scenario of the tensile strength being 10 times smaller than the compressive strength ($r = 0.1$). From the ice field snap shots in Figure 14 it can be seen that within $0.2 < R_c < 0.4$ the sea ice failure regime changes: at $R_c = 0.2$ the failure mode is similar to that of uniaxial compression where the primary failure direction is determined by wing-crack formation (Figure 15) whereas for $R_c \geq 0.4$ the sea ice cover effectively breaks down into floes with only occasional blocks remaining. In this latter case ($R_c > 0.4$), if the wind stress is reduced, then no ice field failure occurs, so that the ice block size cannot be increased by decreasing the wind stress as is in the case for smaller confinement ratios.

[25] In our model a joint breaks in shear rupture at a shear traction linearly dependent on the normal traction, similar to a Coulomb's friction criterion. Shear rupture will be suppressed if the confinement ratio between the large-scale stresses reaches a level where the effective shear stress across any direction becomes zero [e.g., *Schulson*, 2001; *Jaeger and Cook*, 1979],

$$R_c^* = \frac{(\mu^2 + 1)^{1/2} - \mu}{(\mu^2 + 1)^{1/2} + \mu}. \tag{25}$$

For $\mu = 0.6$ used in our model $R_c^* = 0.32$ which corresponds to our numerical results. As the confinement ratio exceeds R_c^* the failure mode changes. From Figure 15 it can be seen that failure starts to occur at arbitrary angles with only a slight bias to the y direction along which compressive failure is easiest. However Figure 16 shows that the failure mode at joints is mainly due to shear rupture with the most probable failure regime determined by the minimum failure energy (15) requiring local divergence. When R_c^* is exceeded, the large-scale wind stress pattern cannot ensure large-scale shear failure anymore. As the wind stress increases, the

compressive strength is still too high to induce any significant failure. However, the irregularity of the floes ensures local shear stress (along the joints) which eventually makes sea ice failure possible locally, so that the ice field breaks up into floes.

[26] If the tensile strength increases (Figure 17) under a homogeneous compressive wind stress gradient (confinement ratio of unity), shear rupture becomes more difficult to attain, and the fraction of compressive failure increases from 12% at $r = 0.1$ to 17%, 44%, 48% and 60% for $r = 0.3$, 0.5, 0.7 and 0.9, respectively. The shear rupture regime is again determined by the minimum failure energy (not shown) similar to other cases with $\delta_r = 0.145$, 0.242 and 0.338 determining the minimum for $r = 0.3$, 0.5 and 0.7. The block size normalized by the shear rupture scale L_f^s increases with r (Figure 18) as the compressive failure determining a larger block scale becomes more important. For a small normalized tensile failure r, the block size is smaller than that given by the shear rupture estimate (22) even though the failure regime is mainly shear. This, we believe, is caused by the fact that while in the case of uniaxial compression the shear rupture work is supplied by the shear elastic strain energy, in the case of uniform convergence the shear-regime failure
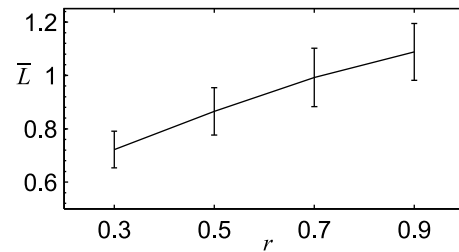

Figure 18. The block size normalized by L_b^s for varying r under uniform convergence ($R_c = 1$). The standard deviation is derived from mean blocks sizes for nine different configurations. Blocks smaller than 10 times the average floe area are filtered out. The estimated block size due to shear rupture only, L_b^s, is 33.35, 37.89, 41.22, and 43.89 km for the relative tensile strength $r = 0.3$, 0.5, 0.7, and 0.9, respectively ($U_{wind} = 5$ m s^{-1}).
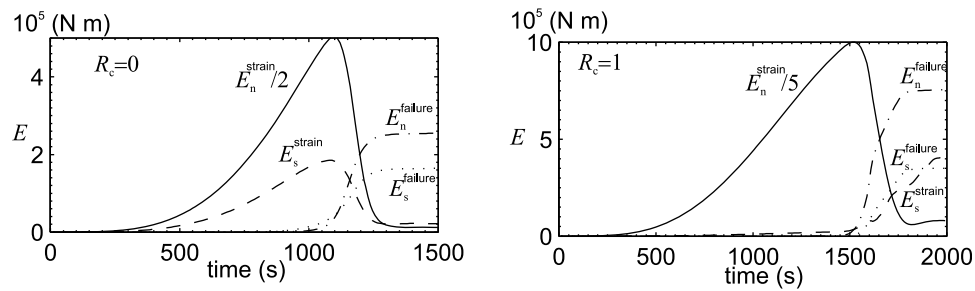
Figure 19. The stored elastic strain energy normal to the joints (solid line) and tangential to the joints (dashed line) versus time for a particular ice field configuration shown in Figures 3 and 14. The accumulated failure (elastic) energy normal to the joint (dot-dashed line) and tangential to the joints (dotted line) are also shown for comparison. (left) The uniaxial compression case ($R_c = 0$). (right) The uniform convergence case ($R_c = 1$) for $U_{wind} = 5$ m s^{-1}.

work is supplied by normal elastic strain energy during failure due to small-scale irregularity of floe shape. From Figure 19 it can be seen that during uniaxial compression both normal and shear strain energy (calculated as work done by elastic deformation over all joint segments that remain unbroken) grow until failure starts, and during failure they both decrease contributing to normal and shear rupture energies that, in turn, grow. In uniform compression the normal strain energy mainly grows, however after failure both normal and shear rupture energies (given by (14) integrated over all broken joint segments) increase, similarly to the uniaxial compression case. This implies that part of the normal strain energy is converted into shear rupture energy. The normal strain energy is higher than the shear strain energy. Therefore if a higher normal strain energy rate is accounted for instead of the lower shear-failure strain rate in (23), then the block size scale would be smaller.

4. Conclusions

[27] A Coulomb shear rupture mechanism for crack formation similar to that found in the laboratory [*Schulson and Nickolayev*, 1995] was incorporated into the sea ice discrete element model of *Hopkins et al.* [2004]. The original model included only compressive and tensile failure of interfloe joints and produced predominantly rectilinear-shaped floe aggregates, which is in contrast to many observations of diamond-shaped floe aggregates in the Arctic. As wind exerts drag on the floes, the floes move and their displacement leads to accumulation of elastic strain energy in the connecting viscous elastic joints. The mutual floe displacement is roughly uniform if the wind stress gradient is constant. The shear strength is related to a particular amount of mutual floe displacement tangential to the edge and is linearly dependent on the elastic force normal to the edge. In particular, a compressive normal elastic force suppresses shear rupture. When the stress reaches the compressive, tensile or shear strengths, local failure occurs and a crack is initiated. Further increase in the elastic strain energy is converted into crack propagation, delineating floe aggregates of a size determined by competition between the rate of crack propagation and the elastic relaxation wave speed. In all cases considered here it has been found that while there is a large degree of variability in shear rupture regimes, the most probable scenario is that when the mini-

mum failure energy is attained, which involves local opening. This minimum failure work was used in our aggregate size evaluation.

[28] In our standard case scenario we consider a tensile strength 10 times smaller than the compressive strength. In this case, when the wind stress describes uniaxial compression, the ice field breaks up into elongated aggregates delineated by cracks with a bimodal maxima distribution at angles determined by the critical flaw angle in the wing crack theory, $\tan(2\theta) = 1/\mu$. The aggregates are roughly diamond shaped and are surrounded by smaller floes in damage zones. As the wind stress gradient increases, the elastic strain energy grows faster leading to a quicker crack propagation speed per unit area, and consequently smaller generated ice block sizes. At the same time the blocks become less anisotropic as their size becomes comparable with the floe size so that there are fewer available floe joints for the crack to propagate along. The aggregate scale found based on minimum failure work agrees with the block size found from simulations. Similar to *Hopkins and Thorndike* [2006] and different observations [*Rothrock and Thorndike*, 1984; *Weiss*, 2003; *Weiss and Marsan*, 2004] our model produces a power law distribution of smaller-size ice block numbers versus their area. A simple model that associates the energy necessary to form a block to the probability of finding it could explain the power exponent.

[29] As the tensile strength increases relative to the compressive strength under uniaxial compressive wind stress, the block size increases as shear rupture becomes harder to attain and compressive failure becomes more important, determining a higher failure energy and slower crack propagation speed per unit area. The generated ice blocks also become elongated perpendicular to the compression direction as the emerging compressive failure is more likely across the compressive direction. The typical aggregate size in this case is estimated by assuming that the length scale along the compressive direction is determined by compressive failure, while the length scale across the compression direction is determined by the mean failure angle. The mean block size as a square root of the product of these length scales then suitably describes the simulated aggregate size as the tensile strength approaches the compressive strength.

[30] If in the standard case scenario the confinement ratio of the wind stress gradient increases, the failure mode changes when the confinement ratio is between 0.2 and 0.4,

which is in agreement with the theoretical prediction of failure mode change at the critical confinement ratio of 0.32 for the shear rupture coefficient $\mu = 0.6$. Below this range the failure occurs similar to the uniaxial compression case, where diamond-shaped aggregates are produced. Above this range the ice field starts to fail isotropically since the Coulomb failure criterion cannot be attained on the large scale. Local stress anomalies arising due to the irregularity of the floes lead to shear rupture of the ice field with block sizes smaller than that predicted by the shear rupture estimates. We argue that this is due to conversion of a higher, normal strain energy to shear rupture energy. As the tensile strength increases, compressive failure become more prevalent and the aggregate size increases.

[31] Our simulations have shown that shear rupture is an important factor in determining sea ice block shape and size. The observed diamond shape of the blocks can be produced by low confinement ratio wind stress patterns if sea ice tensile strength is much smaller than the compressive strength. When the confinement ratio increases, the blocks become isotropic. When the tensile strength increases, the block shape also changes becoming elongated across the uniaxial compression direction. While the tensile strength of sea ice is still ambiguous, results of our, albeit idealized, simulations show that in order for the diamond shape structures to exist, the tensile strength should be much smaller than the compressive strength.

References

Ashby, M. F., and S. D. Hallam (1986), The failure of brittle solids containing small cracks under compressive stress states, *Acta Metall. Mater.*, *34*, 497–510.

Dempsey, J. D., R. M. Adamson, and S. V. Mulmule (1999), Scale effects on the in situ tensile strength and fracture of ice: Part II. First-year sea ice at Resolute, N.W.T., *Int. J. Fracture*, *95*, 347–366, doi:10.1023/A:1018650303385.

Erlingsson, B. (1991), The propagation of characteristics in sea-ice deformation fields, *Ann. Glaciol.*, *815*, 73–80.

Evans, R., and N. Untersteiner (1971), Thermal cracks in floating ice sheets, *J. Geophys. Res.*, *79*(3), 694–703, doi:10.1029/JC076i003p00694.

Hopkins, M. A. (1994), On the ridging of intact ice, *J. Geophys. Res.*, *99*(C8), 16,351–16,360, doi:10.1029/94JC00996.

Hopkins, M. A. (1996), On the mesoscale interaction of lead ice and floes, *J. Geophys. Res.*, *101*, C01032, doi:10.1029/2003JC001855.

Hopkins, M. A., and A. S. Thorndike (2006), Floe formation in arctic sea ice, *J. Geophys. Res.*, *111*, C11S23, doi:10.1029/2005JC003352.

Hopkins, M. A., and J. Tuhkuri (1999), Compression of floating ice fields, *J. Geophys. Res.*, *104*(C7), 15,815–18,825.

Hopkins, M. A., S. Frankenstein, and A. S. Thorndike (2004), Formation of an aggregate scale in Arctic sea ice, *J. Geophys. Res.*, *109*, C01032, doi:10.1029/2003JC001855.

Jaeger, J. C., and N. G. W. Cook (1979), Elasticity and strength of rock, in *Fundamentals of Rock Mechanics*, edited by J. C. Jaeger and N. G. W. Cook, chap. 4, pp. 95–100, Chapman and Hall, London.

Kovacs, A., and D. S. Sodhi (1980), Shore ice pile-up and ridge-up: Field observations, models, theoretical analyses, *Cold Reg. Sci. Technol.*, *2*, 209–288.

Kwok, R. (2001), Arctic Ocean sea ice deformation from SAR ice motion: Linear kinematic features, *Tech. Rep. JPL D-21524*, Jet Propul. Lab., Pasadena, Calif.

Lewis, J. K., and J. A. Richter-Menge (1998), Motion-induced stresses in pack ice, *J. Geophys. Res.*, *103*(C10), 21,831–21,843.

Lishman, B., P. Sammonds, D. Feltham, and A. Wilchinsky (2009), The rate and state dependence of sea ice friction, paper presented at 20th International Conference on Port and Ocean Engineering Under Arctic Conditions, Luleå Univ. of Technol., Lulea, Sweden, 9–12 June.

Overland, J., S. L. McNutt, S. Salo, and S. S. Li (1998), Arctic sea ice as a granular plastic, *J. Geophys. Res.*, *103*(C10), 21,845–21,867.

Richter-Menge, J. A., and K. F. Jones (1993), The tensile stress of first-year sea ice, *J. Glaciol.*, *39*, 609–618.

Rothrock, D. A., and A. S. Thorndike (1984), Measuring the sea ice grain size distribution, *J. Geophys. Res.*, *89*(C9), 6477–6486, doi:10.1029/JC089iC04p06477.

Schulson, E. M. (2001), Brittle failure of ice, *Eng. Fract. Mech.*, *68*, 1839–1887, doi:10.1016/S0013-7944(01)00037-6.

Schulson, E. M. (2004), Compressive shear faults within arctic sea ice: Fracture on scales large and small, *J. Geophys. Res.*, *109*, C07016, doi:10.1029/2003JC002108.

Schulson, E. M., and O. Y. Nickolayev (1995), Failure of columnar saline ice under biaxial compression: Failure envelopes and the brittle-to-ductile transition, *J. Geophys. Res.*, *100*(B11), 22,383–22,400.

Schulson, E. M., A. L. Fortt, D. Iliescu, and C. E. Renshaw (2006), On the role of frictional sliding in the compressive fracture of ice and granite: Terminal vs. post-terminal failure, *Acta Mater.*, *54*, 3923–3932, doi:10.1016/j.actamat.2006.04.024.

Walter, B. A., J. Overland, and P. Turet (1995), A comparison of satellite-derived and aircraft-measured regional surface sensible heatfluxes over the Beaufort Sea, *J. Geophys. Res.*, *100*(C3), 4585–4591, doi:10.1029/94JC02653.

Weiss, J. (2001), Fracture and fragmentation of ice: A fractal analysis of scale invariance, *Eng. Fract. Mech.*, *68*, 1975–2012, doi:10.1016/S0013-7944(01)00034-0.

Weiss, J. (2003), Scaling of fracture and faulting of ice on earth, *Surv. Geophys.*, *24*, 185–227, doi:10.1023/A:1023293117309.

Weiss, J., and D. Marsan (2004), Scale properties of sea ice deformation and fracturing, *Surv. Geophys.*, *5*, 735–751, doi:10.1016/j.crhy.2004.09.005.

Weiss, J., and E. M. Schulson (2007), Sea ice rheology from in situ, satellite and laboratory observations: Fracture and friction, *Earth Planet. Sci. Lett.*, *255*, 1–8, doi:10.016/j.epsl.2006.1.033.

Weiss, J., and E. M. Schulson (2009), Coulombic faulting from the grain scale to the geophysical scale: Lessons from ice, *J. Phys. D Appl. Phys.*, *42*, 214017, doi:10.1088/0022-3727/42/21/214017.

Wilchinsky, A. V., and D. L. Feltham (2006), Modelling the rheology of sea ice as a collection of diamond-shaped floes, *J. Non Newtonian Fluid Mech.*, *138*, 22–32, doi:10.1016/j.jnnfm.2006.05.001.

D. L. Feltham and A. V. Wilchinsky, Centre for Polar Observation and Modelling, National Centre for Earth Observation, University College London, Gower Street, London WC1E 6BT, UK. (dlf@cpom.ucl.ac.uk; aw@cpom.ucl.ac.uk)

M. A. Hopkins, CRREL, U.S. Army Corps of Engineers, 72 Lyme Rd., Hanover, NH 03755, USA. (mark.a.hopkins@usace.army.mil)